# Tunable Properties of Novel Ga$_2$O$_3$ Monolayer for Electronic and Optoelectronic Applications

Yikai Liao,[∇] Zhaofu Zhang,*[,∇] Zhibin Gao, Qingkai Qian, and Mengyuan Hua*

Read Online

ACCESS | Metrics & More | Article Recommendations | Supporting Information

**ABSTRACT:** A novel two-dimensional (2D) Ga$_2$O$_3$ monolayer was constructed and systematically investigated by first-principles calculations. The 2D Ga$_2$O$_3$ has an asymmetric configuration with a quintuple-layer atomic structure, the same as the well-studied $\alpha$-In$_2$Se$_3$, and is expected to be experimentally synthesized. The dynamic and thermodynamic calculations show excellent stability properties of this monolayer material. The relaxed Ga$_2$O$_3$ monolayer has an indirect band gap of 3.16 eV, smaller than that of $\beta$-Ga$_2$O$_3$ bulk, and shows tunable electronic and optoelectronic properties with biaxial strain engineering. An attractive feature is that the asymmetric configuration spontaneously introduces an intrinsic dipole and thus the electrostatic potential difference between the top and bottom surfaces of the Ga$_2$O$_3$ monolayer, which helps to separate photon-generated electrons and holes within the quintuple-layer structure. By applying compressive strain, the Ga$_2$O$_3$ monolayer can be converted to a direct band gap semiconductor with a wider gap reaching 3.5 eV. Also, enhancement of hybridization between orbitals leads to an increase of electron mobility, from the initial 5000 to 7000 cm$^2$ V$^{-1}$ s$^{-1}$. Excellent optical absorption ability is confirmed, which can be effectively tuned by strain engineering. With superior stability, as well as strain-tunable electronic properties, carrier mobility, and optical absorption, the studied novel Ga$_2$O$_3$ monolayer sheds light on low-dimensional electronic and optoelectronic device applications.

**KEYWORDS:** Ga$_2$O$_3$ monolayer, intrinsic dipole, carrier mobility, strain engineering, first-principles calculations
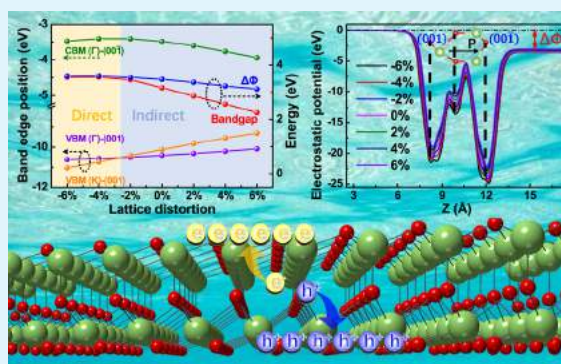
## 1. INTRODUCTION

Wide-band-gap semiconductors such as ZnO, GaN, AlN, and Ga$_2$O$_3$ have attracted increasing attention for optoelectronic and power electronic applications.[1] Among them, Ga$_2$O$_3$, especially in the form of single-crystal bulk or thin films, has been investigated extensively for its attractive material properties, such as an ultrawide band gap (∼4.8 eV),[2] outstanding breakdown field (8 MV/cm), and good chemical stability. In addition, common methods of crystal growth including the Czochralski method (CZ) and edge-defined film fed (EFG) are feasible for bulk Ga$_2$O$_3$, promoting the wide investigations of $\beta$-Ga$_2$O$_3$.[2]

Ever since the graphene monolayer was successfully synthesized, two-dimensional (2D) materials such as transition-metal dichalcogenides (TMDs) and hexagonal boron nitride have become the up-to-date focal point and the mainstream of scientific research. In contrast to the three-dimensional (3D) materials with a very long history of study, 2D materials still need to be explored. To expedite the process, theoretical calculations by tools such as density functional theory (DFT) have been widely employed to study certain structures or material applications. The high-throughput method has been used as an efficient access to screen materials with certain desired properties for potential applications.[3,4]

However, the cost to cover an enormous number of potential materials could be huge. An alternative method is obtaining the material structure from a known one by atomic replacement, which has been widely used to create and compare compounds in the same element groups with the same or similar structure and serves as a guide for experimental chemists to explore new materials and applications.[5,6] Compared with their 3D counterparts, 2D materials exhibit interesting and outstanding properties such as tunable band gap by strain and high surface-area-to-volume ratio, benefitting to their wider application ranges over the bulk counterparts. Since the properties of 2D materials can be tuned by strain-induced lattice distortion, one widely studied application is flexible electronic devices, by changing the performance of devices via applying external strain, i.e., bending, starching, or compressing the substrates.[7] For example, a 2D material-based photodetector is able to possess strain-tunable wavelength selectivity of photodetec-

tion.[8] For 2D material-based power transistors, strain-induced tunable properties such as effective mass and Schottky barrier height are significant for device performance.[9] Thus, to delve into the uncharted territory of wide-band-gap semiconductors, DFT research studies on their 2D structures are proceeding rapidly and productively. For example, Claeyssens et al.[10] theoretically predicted the existence of stable graphene-like ZnO (g-ZnO) by density functional theory and Tusche et al.[11] successfully observed the unreconstructed planar sheet of g-ZnO monolayers. Zhuang et al.[12] predicted and investigated the energetic and dynamic stability of 2D GaN by DFT, which was later experimentally synthesized via migration-enhanced encapsulated growth (MEEG).[13]

Compared with ZnO and GaN monolayers, the study on 2D $Ga_2O_3$ still remains the very infant step. Theoretically, as a start, Van de Walle et al.[14] tried to model the monolayer $Ga_2O_3$ structure by reducing the thickness of the monoclinic $\beta$-$Ga_2O_3$ unit cell (12 Å) along the [100] direction down to half (6 Å). Until now, some progress has been made based on Van de Walle's model. Su et al.[15,16] studied its hydrogen-passivated structure and demonstrated its surprisingly high electron mobility (~25 000 $cm^2$ $V^{-1}$ $s^{-1}$) and optoelectronic properties. Wei et al.[17] revealed the influence of surface vacancies on its electrical and optical properties. Experimentally, even though mechanical exfoliation from bulk $\beta$-$Ga_2O_3$ is a feasible way to obtain $Ga_2O_3$ nanomembranes with a thickness less than 100 nm, which can to some extent be regarded as quasi-2D materials, their physical properties are still close to the bulk $\beta$-$Ga_2O_3$ because their thicknesses are far away from the angstrom scale.[18,19] What is more, despite the fact that exfoliation energy along the [100] direction is much lower than others,[15,20] the covalent bond is still so strong that it is difficult to slice monoclinic $\beta$-$Ga_2O_3$ down into nanoscale and obtain the authentic 2D monolayer in experiments. Besides, it should be noted that once scaled down to monolayer thickness, the structure of the monolayer does not always maintain the same as its bulk counterpart.[11,13] More importantly, it still remains to be experimentally verified whether the hydrogen-passivated 2D $\beta$-$Ga_2O_3$ monolayer can be synthesized. Thus, the feasibility of a 2D $Ga_2O_3$ monolayer based on monoclinic $\beta$-$Ga_2O_3$ remains controversial and the existence of monolayer $Ga_2O_3$ in other crystal forms is still worth investigating.

In spite of the very limited investigations on the 2D $Ga_2O_3$ monolayer, researchers have focused on its 2D III−VI van der Waals (vdW) family members for their attractive properties and outstanding application potentials such as optoelectronics[21] and ferroelectrics.[22,23] Some of them have been successfully synthesized by experiments.[24] Among those, 2D $\alpha$-$In_2Se_3$ with the crystal structure of ferroelectric-zinc blende (FE-ZB′) phase is theoretically proven stable[22] and has been successfully fabricated by experiments through mechanical exfoliation[21] or van der Waals epitaxy.[24] Interestingly, its asymmetric atomic configuration leads to the existence of unusual polarization, broadening its application ranges to water splitting,[5,25] gas sensing,[26] and piezoelectricity,[27] indicating that this $In_2Se_3$ atomic configuration is of great importance in research and development. Thus, it is of technological interest to study the properties of the $Ga_2O_3$ monolayer with the same configuration as $\alpha$-$In_2Se_3$.

It is noted that, despite the relatively stronger ionic bond, the exfoliation of metal oxide is not that hard. One typical example is that $\beta$-$Ga_2O_3$ can be exfoliated, benefitting from weak Ga−O bonds along the [100] direction.[15,18,20] Apart from the 2D $Ga_2O_3$ monolayer, a considerable amount of 2D metal oxides has already been experimentally synthesized, such as 2D $WO_3$, 2D $MoO_2$, and 2D $TiO_2$.[28] Theoretically, some researchers have proved that 2D metal oxides, such as GaO, InO,[29] and $MoO_2$,[30] will have the same structure as metal selenides. Experimentally, significant progress on the oxidation of 2D vdW semiconductor materials such as $HfS_2$[31] and $TaSe_2$[32] has been made to synthesize their monolayer oxides. In fact, some researchers have successfully converted non-van der Waals (non-vdW) solids to 2D vdW chalcogenides in experiments.[33] Since $Ga_2O_3$ shares the same element groups as $In_2Se_3$, it is reasonable to infer that the $Ga_2O_3$ monolayer with the lattice structure of 2D $\alpha$-$In_2Se_3$ can be experimentally synthesized by similar methods such as epitaxial growth or controlled oxidation.[24,31]

In this work, we conducted a pioneering investigation on the properties of the novel $Ga_2O_3$ monolayer, which has 2D $\alpha$-$In_2Se_3$ geometry, by first-principles calculation. This novel $Ga_2O_3$ monolayer shows excellent dynamic and thermodynamic stability. The $Ga_2O_3$ monolayer is identified to be an indirect band gap semiconductor with a band gap of 3.16 eV and an electron mobility of ~5000 $cm^2$ $V^{-1}$ $s^{-1}$. With biaxial strain engineering, the tunable band gap, intrinsic dipole, carrier transport ability, and optical properties were studied. The direct−indirect transition of band gap has been observed with different lattice distortions. The compressed $Ga_2O_3$ monolayer (−4% lattice distortion) is found to be a direct band gap semiconductor with a wide band gap (~3.5 eV) and outstanding electron mobility (~7000 $cm^2$ $V^{-1}$ $s^{-1}$), while the stretched $Ga_2O_3$ monolayer has a good solar radiation absorption capability. The considerable electrostatic potential difference between the top and bottom surfaces, which is induced by the intrinsic dipole in the asymmetric structure, is able to boost the separation of photon-generated holes and electrons. These tunable properties suggest that the $Ga_2O_3$ monolayer has great application potentials for flexible nanoscale electronic devices and solar energy conversion.

## 2. COMPUTATIONAL METHODS

The calculations were conducted based on density functional theory, as implemented in the Vienna ab initio simulation package (VASP).[34] The projector augmented wave (PAW)[35] pseudopotential was used. The PAW potential is capable of precisely handling the difficult and complex cases such as strong magnetic moments and large electronegativity differences, whose reliability is better than ultrasoft pseudopotential[36] and precision is comparable with norm-conserving.[37] The use of the PAW pseudopotentials addresses the problem of inadequate description of the wavefunctions in the core region common to other pseudopotential approaches.[38] A planewave cutoff energy of 450 eV was used. This cutoff energy was tested effective for convergence by comparing the calculated band gap with a much higher cutoff energy of 700 eV, and a negligible difference of 1 meV was found. The total energy difference is within 1 meV/atom. Even though the Perdew−Burke−Ernzerhof (PBE) version of generalized gradient approximation (GGA-PBE)[39] is widely used for calculations, it suffers from the slightly overestimated lattice constant and unavoidable band gap narrowing problems.[40] To guarantee the precise property descriptions of this novel material, the Heyd−Scuseria−Ernzerhof (HSE) hybrid functional[41] was employed (with a default mixing fraction) throughout this work, including the lattice structure optimization and electronic and optical properties. The convergence criteria were set to be $1 \times 10^{-5}$ eV/atom for self-consistent electronic loop and 0.02 eV/Å for the residual forces on each atom. A $9 \times 9 \times 1$ k-mesh grid was used. The vdW correction
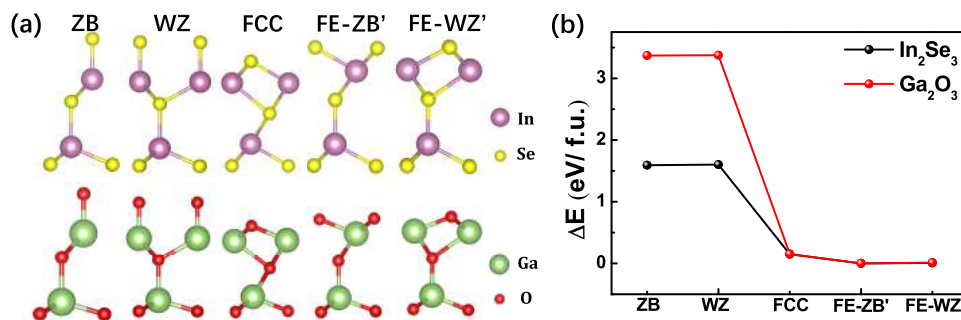
**Figure 1.** (a) Atomic structures of five different $In_2Se_3$ and $Ga_2O_3$ phases. (b) Total energy comparison, with the total energy of the most stable FE-ZB′ phase set to be 0 eV.

with Grimme's scheme (DFT-D3) was considered.[42] A 15 Å thickness vacuum layer was adopted to avoid interaction between layers.[43] A linear dipole correction is added to the local potential to correct the errors introduced by the periodic boundary conditions so that the work function and band edges can be evaluated individually. The band structure was analyzed with VASPKIT, a pre- and postprocessing program for the VASP code.[44]

The phonon dispersions were calculated using a linear response approach on the basis of density functional perturbation theory[45] with the Phonopy code,[46] and the convergence criteria were set to be $5 \times 10^{-7}$ eV/atom for energy and 0.001 eV/Å for force. The thermostability of the $Ga_2O_3$ monolayer was evaluated by ab initio molecular dynamic simulation (AIMD) within a $3 \times 3$ supercell. The Anderson thermostat was employed, with a time step of 1 fs.

The strained structures were generated by adjusting the cell lattice constants away from their relaxed values. To optimize the structures under different strains, only the atomic coordinates are allowed to relax, with the cell vectors fixed.[47]

## 3. RESULTS AND DISCUSSION

**3.1. Structural and Electronic Properties.** To demonstrate the feasibility of the proposed $Ga_2O_3$ monolayer, based on several $In_2Se_3$ structures, including zinc blende (ZB), wurtzite (WZ), FCC, FE-ZB′, and FE−WZ′ phases discussed in Ding's work,[22] we modeled various $Ga_2O_3$ structures with these phases for comparison. The structures and relative energies are shown in Figure 1. Similar to $In_2Se_3$, $Ga_2O_3$ with the FE-ZB′ structure has the lowest total energy among all of the structures, as shown in Figure 1b, proving that this $Ga_2O_3$ phase is the thermodynamic ground state and is promising to be synthesized without other-phase byproducts. Thus, this work will focus on the discussion of the $Ga_2O_3$ monolayer with the FE-ZB′ configuration. The optimized lattice parameters are $a = b = 3.08$ Å by GGA-PBE and $a = b = 3.04$ Å by the HSE functional, with $\alpha = \beta = 90°$ and $\gamma = 120°$, agreeing with the well-known conclusion that GGA-PBE produces the slightly overestimated lattice constant.[40] The lattice constant of $Ga_2O_3$ is much smaller than that of $\alpha$-$In_2Se_3$ (4.11 Å),[5] owing to the smaller atomic radii of gallium and oxygen. Since HSE offers a better prediction of semiconducting behavior than the local or semilocal functionals,[40] the optimized structure obtained by the HSE functional is employed for further electronic and optical discussions.

The geometries of $Ga_2O_3$ monolayer are shown as insets of the right panel in Figure 2a. The same as $\alpha$-$In_2Se_3$ and other 2D $M_2X_3$ (M = Al, Ga, In; X = S, Se, Te) family members,[5] the $Ga_2O_3$ monolayer is stacked in the atomic layer sequence of O−Ga−O−Ga−O, forming the quintuple layer consisted of covalently bonded gallium and oxygen triangular lattices.[23,24] We also compared geometries of the $Ga_2O_3$ monolayer with
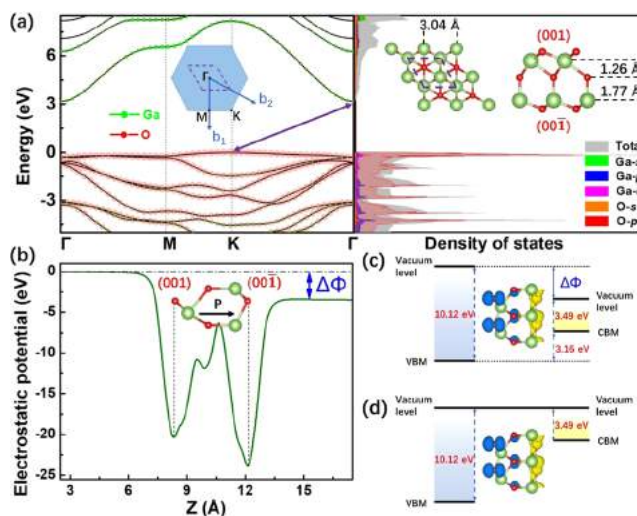


**Figure 2.** (a) Band structure (left) and DOS (right) of the $Ga_2O_3$ monolayer with the FE-ZB′ phase by HSE. In the left panel, the green and red dots represent the contribution strength from gallium and oxygen orbitals, respectively. The purple arrow shows the indirect band gap from VBM (K) to CBM (Γ). In the right panel, the purple dashed parallelogram indicates the primitive cell. (b) Electrostatic potential of the relaxed $Ga_2O_3$ monolayer along the z direction. The direction of spontaneous polarization is indicated by the black arrow. Band alignment of the $Ga_2O_3$ monolayer with (c) different vacuum levels and (d) aligned vacuum levels. Insets show the spatial charge distributions of CBM (yellow) and VBM (blue), respectively. The (001) and (00$\bar{1}$) surfaces are defined in the insets in (a) and (b).

known monoclinic $\beta$-$Ga_2O_3$ in Figure S1 with the same functional and calculation settings. The Ga−O bond lengths of the $Ga_2O_3$ monolayer here are comparable with those of the monoclinic $\beta$-$Ga_2O_3$, which can stably exist in nature, indicating the stable Ga−O connection in the $Ga_2O_3$ monolayer.

The calculated band gap of the $Ga_2O_3$ monolayer is 3.16 eV by the HSE functional, as demonstrated in Figure 2a. The $Ga_2O_3$ monolayer is an indirect band gap semiconductor with the conduction band minimum (CBM) at Γ point and the valance band maximum (VBM) at K point. Oxygen, especially the O p orbital, contributes most to the valance band regions near VBM, while gallium contributes more to the conduction band. Also, hybridization between different orbitals can be seen in both CBM and VBM. The CBM is composed of Ga s and O s with little Ga $p_z$ and O $p_z$ orbitals, VBM at K point is mainly composed of O $p_z$ with little O $p_x$ and O $p_y$ and negligible Ga p and Ga d orbitals, and VBM at Γ point is mainly composed of
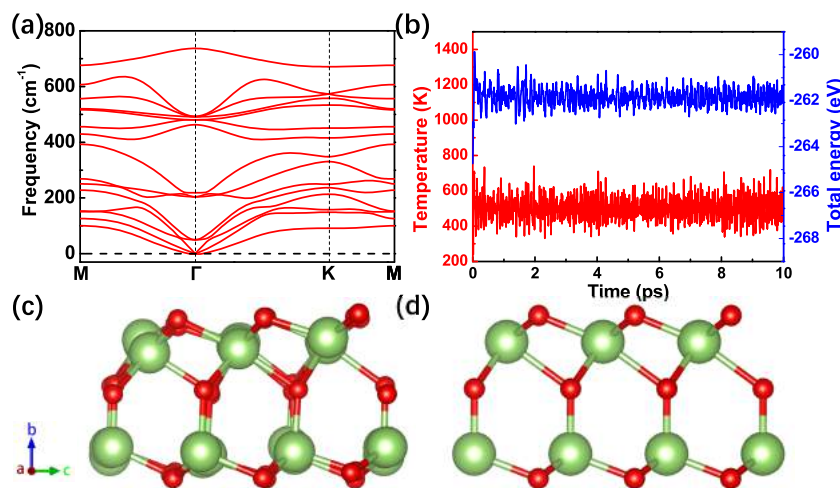
**Figure 3.** (a) Phonon dispersion spectrum of the Ga$_2$O$_3$ monolayer. (b) Evolution of temperature (red, left axis) and total energy (blue, right axis) with time during AIMD simulations. Atomic structures of the Ga$_2$O$_3$ (3 × 3) supercell after (c) 10 ps AIMD simulation at 500 K and further (d) geometry relaxation.

O p$_x$ and O p$_y$ with negligible Ga p orbitals (Ga p$_x$ and Ga p$_y$) and Ga d orbitals (Ga d$_{xy}$ and Ga d$_{x^2-y^2}$), as verified from the orbital-resolved band structure in Figure S2. The first Brillouin zone with high-symmetric points of Ga$_2$O$_3$ monolayer is shown in the inset of Figure 2a.

When studying the electronic properties of the Ga$_2$O$_3$ monolayer, the asymmetric atomic configuration should be taken into consideration. Analogous to other polar 2D materials such as Janus TMDs,[6,48] there exists an intrinsic electric field in 2D M$_2$X$_3$ materials due to the breaking of centrosymmetry;[5,22] thus, intrinsic dipole[49,50] forms even within the pristine materials. The electrostatic potential curve of the Ga$_2$O$_3$ monolayer along the z direction is plotted in Figure 2b. ΔΦ is defined as the vacuum level difference (i.e., the offset in the electrostatic potential curves) between the top and bottom surfaces, which were named as (001) and (00$\bar{1}$) surfaces, respectively,[5] as shown in the insets of Figure 2. Even though the top O−Ga layers and bottom Ga−O layers are symmetric, the bonding orientation of the middle oxygen layer leads to a much shorter out-of-plane distance between the middle O and top Ga (1.26 Å) than that between the middle O and bottom Ga bond (1.77 Å) (Figure 2a). Thus, the top O−Ga−O trilayer (thickness of 1.99 Å, closer to the (001) surface) is supposed to have larger electronegativity, making it the negative charge center, while the bottom O−Ga−O trilayer (thickness of 2.43 Å, closer to the (00$\bar{1}$) surface) acts as the positive charge center. The spatial separation of positive and negative charge centers introduces intrinsic dipole and thus a built-in electric field. It is similar to Janus TMDs, in which electrostatic potential difference is induced by the difference in electronegativity between the top-most and bottom-most atoms in the trilayered structures.[30,51,52] The existence of ΔΦ between two surfaces is indicated in the band diagram of Figure 2c. If we align the two vacuum levels, the energy band closer to the (00$\bar{1}$) surface would be pulled up and becomes closer to the vacuum level, as shown in Figure 2d. Because of the intrinsic electric field, the band near the opposite surface regions could bend toward opposite directions, leading to the shift of CBM and VBM at two surfaces.[53,54] As a result, CBM and VBM wavefunctions spatially localize at the opposite sides of the Ga$_2$O$_3$ surfaces, as shown in the insets of Figure 2c,d and

later Figure 6. The energy difference between CBM of (00$\bar{1}$) and VBM of (001) is contributed from two parts: band gap energy and electrostatic potential difference (ΔΦ), as shown in Figure 2d.

The structural stability of the Ga$_2$O$_3$ monolayer is of great importance not only for the theoretical prediction of properties but also for synthesizing this novel structure and thus further practical applications. The lattice dynamic stability of the Ga$_2$O$_3$ monolayer is evaluated by the phonon dispersion spectrum, as shown in Figure 3a. No imaginary-frequency phonon mode is observed in the phonon dispersion spectrum, indicating a dynamic stable structure.[15,22] An AIMD simulation at 500 K was conducted for a (3 × 3) supercell to verify its thermostability. After 10 ps high-temperature annealing, no structural corruption was observed (Figure 3c). The temperature and total energy of systems during AIMD calculations fluctuate stably with small ups and downs (Figure 3b), indicating excellent thermostability. An AIMD calculation at 300 K was also evaluated, as shown in Figure S3. After 10 ps high-temperature AIMD simulation, the distorted structure further went through an extra structural relaxation. Surprisingly, it turned out that the distorted structure can return to its original well-symmetrical structure after final relaxation, as shown in Figures 3d and S3b. The AIMD results indicate that the Ga$_2$O$_3$ monolayer shows excellent thermostability at high temperatures, guaranteeing the possible applications in high-temperature ambient such as nanoscale power devices and sensors.

**3.2. Strain-Engineered Band Structures.** Since the Ga$_2$O$_3$ monolayer has a large band gap of ∼3.2 eV, in the UV light region, it is attractive to investigate its application potentials in flexible UV detectors and other possible fields. In flexible devices, strain-induced lattice distortion would modulate the electronic band structure, carrier transport, and optical properties.[47,55] Biaxial strain engineering with a series of lattice distortions from −6 to 6% was applied to the Ga$_2$O$_3$ monolayer, with the strained energy tendency shown in Figure S4a. The relaxed system (no strain condition) has the lowest total energy, which means it is the most stable status. When strain is applied to the lattice, distances between atoms in different layers with the quintuple-layer structure change
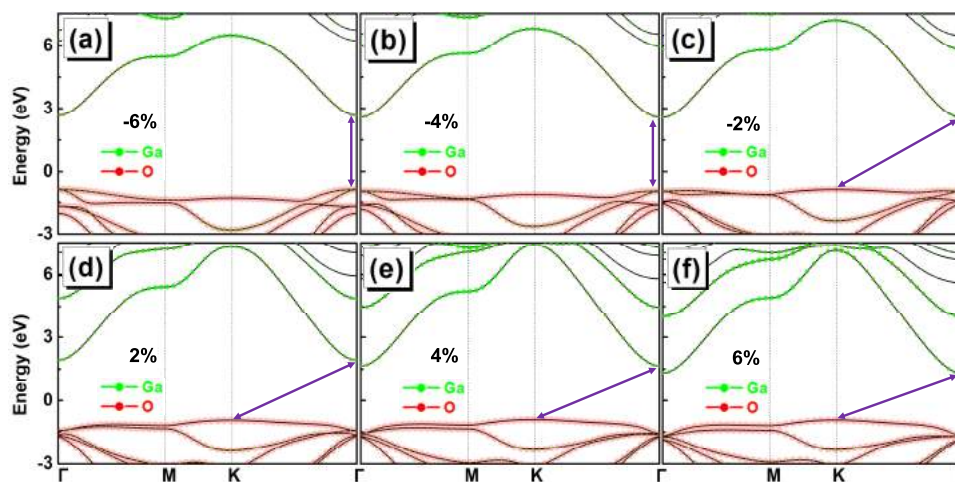
**Figure 4.** Band structure of the Ga$_2$O$_3$ monolayer with lattice distortions of (a) −6%, (b) −4%, (c) −2%, (d) 2%, (e) 4%, and (f) 6%.

correspondingly. Thus, the change of wavefunction overlapping in different layers occurs accordingly, causing the change of total system energy. Besides, it requires more energy to compress the lattice to the distortion of −6% (0.66 eV) than stretch to 6% (0.44 eV), which means it is easier to stretch the Ga$_2$O$_3$ monolayer than to compress it. To release the applied strain, the quintuple-layer thickness of Ga$_2$O$_3$ elongates and shrinks linearly along the $z$ direction when compressive or tensile strains are applied, indicated by the variation of thicknesses in Figure S4b.

The stability of the Ga$_2$O$_3$ monolayer with extreme lattice distortion was also tested using phonon dispersion and AIMD, as shown in Figure S5. There is no imaginary-frequency phonon mode and structural corruption after AIMD in the Ga$_2$O$_3$ monolayer with distortion from −4 to +6%, indicating that the monolayer can maintain its dynamic and thermodynamic stability within this strain range. The compressed Ga$_2$O$_3$ monolayer shows poorer stability than the stretched one, similar to the previous reports.[56] Under −6% compressive strain, the model shows unstable characteristics from both AIMD and phonon dispersion calculations. As a result, we only focus on from −4% to 6% lattice distortion in the following discussions. Since a large strain of ∼6% in the 2D material is already obtained in the experiment,[57] our work is referable in future applications. Despite the tunable properties by strain engineering are desirable for future applications in flexible devices, the main claim in this work is still the availability and the basic properties of this novel Ga$_2$O$_3$ monolayer.

Figure 4 presents the strain-dependent band structure of the Ga$_2$O$_3$ monolayer. The direct−indirect transition of band gap is observed from compressive strain to tensile strain. CBM remains at Γ point, while VBM changes from Γ to K point with decreasing compressive strain and increasing tensile strain. Since there exist two vacuum levels at opposite surfaces of the Ga$_2$O$_3$ monolayer, we plotted the shift of band gap and band edges versus two vacuum levels, respectively, in Figure S6. However, due to polarization, CBM tends to locate closer to the (00$\bar{1}$) surface, while VBM to the (001) surface. Thus, the energy change of CBM with respect to the vacuum level of the (00$\bar{1}$) surface and the energy change of VBM to that of the (001) surface are summarized in Figure 5 to precisely study the shift of band edges. With decreasing compressive strain (from −4% lattice distortion to zero strain) and increasing tensile strain (from zero strain to +6% lattice distortion), energy
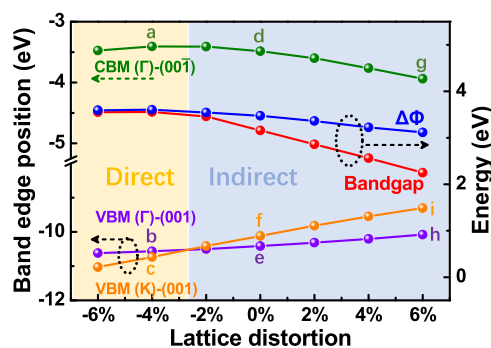


**Figure 5.** Shift of band edges (green, orange, and purple dots and lines, left axis), band gap, and ΔΦ (red and blue, right axis) versus lattice distortions. The energy of CBM is calculated with respect to the vacuum level of the (00$\bar{1}$) surface, while that of VBM to the vacuum level of the (001) surface. The yellow area (left) shows the direct band gap characteristic, while the gray area (right) shows the indirect band gap characteristic. Dots with labels of a−i correspond to wavefunctions in Figure S8a-i, respectively.

positions of both VBM at Γ and K points keep increasing, with a variation of VBM (K) being more rapid than VBM (Γ). As a consequence, the energy position of VBM at K point surpasses that of VBM at Γ point at about −2.5% lattice distortion, leading to the transition from the direct band gap to the indirect one. What is more, the band gap value reaches a maximum at a lattice distortion of −4% (Figure 5) and then keeps narrowing down due to the opposite trends of a shift of CBM (Γ) and VBM (K). We also calculated the strain-dependent band gap values by PBE and GW$_0$[58] functionals for comparison (Figure S7). All three functionals show the same variation of band gap versus lattice distortion. Clearly, the PBE functional results in underestimated band gap values. Taking excited state into consideration, GW$_0$ results in higher band gap values than the HSE case, similar to the In$_2$Se$_3$ case.[5] Considering the computational consumption, we only adopt the HSE hybrid functional in this work.

To better investigate the origins of the variation trend of CBM and VBM with lattice distortion changing, we studied the wavefunction distributions of CBM and VBM, as shown in Figure S8. CBM at Γ point (Figure S8a,d,g), labeled as a, d, and g in Figure 5, respectively, is mainly composed of in-plane antibonding of top Ga−O layers between Ga s, O s, Ga p$_z$, and
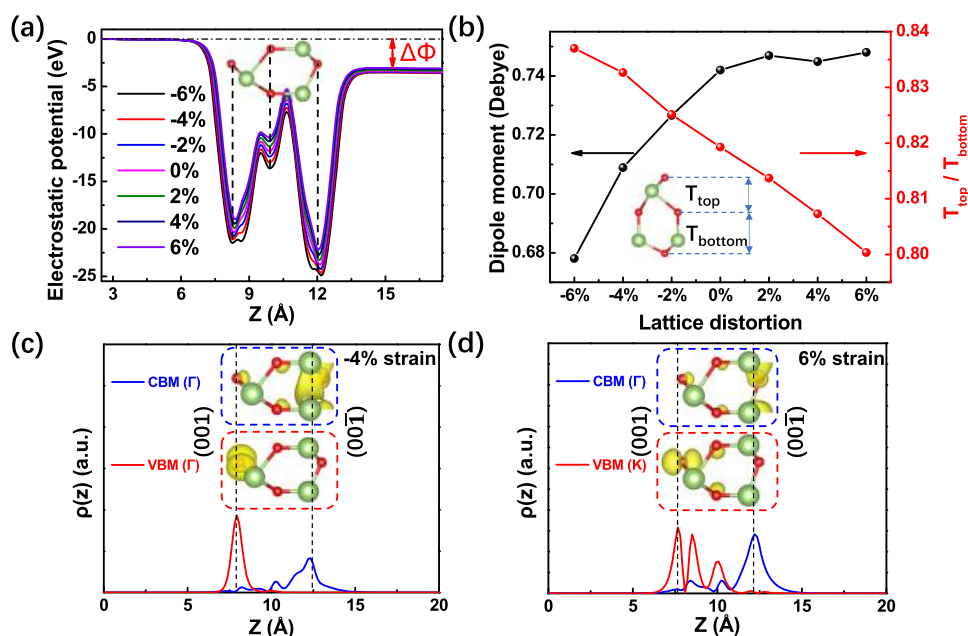
**Figure 6.** (a) Electrostatic potential of the $Ga_2O_3$ monolayer along the $z$ direction. (b) Variation of the dipole moment (black, left axis) and relative thickness of the top O−Ga−O trilayer ($T_{top}$) and bottom O−Ga−O trilayer ($T_{bottom}$) (red, right axis) versus lattice distortions. Charge distribution of the $Ga_2O_3$ monolayer at lattice distortion of (c) −4% and (d) 6% along the $z$ direction. In (c) and (d), the inset figures in blue and red rectangles show spatial charge distribution of CBM and VBM, respectively, with the same isosurface level.

O $p_z$ orbitals, indicated by orbital-projected band structure in Figure S2. This orbital hybridization characteristic of CBM (Γ) is similar to the monoclinic $\beta$-$Ga_2O_3$ monolayer.[16] As the compressive strain keeps decreasing (more positive) and finally undergoes a transition into tensile strain, the in-plane bond lengths increase. According to the Heitler−London exchange energy model, increasing atomic distance leads to a decrease of antibonding energy.[59] However, the in-plane bonding characteristic (the blue beltlike areas in Figure S8a,d,g) weakens, leading to higher CBM edge.[59] Thus, because of the competition of in-plane bonding and antibonding, the energy position of CBM (Γ) increases first until reaching −2% distortion and then decreases with strain changing from compressive to tensile. Similar competition of bonding and antibonding and the variation of CBM can also be seen in other 2D materials.[60] With strain becoming more positive, the VBM (Γ) edge is pushed upward because of the decreasing in-plane bonding characteristic (more clearly demonstrated by the in-plane connected areas in Figure S9) in top O vicinity shown in Figure S8b,e,h (labeled as b, e, and h in Figure 5, respectively).[59]

As for VBM (K) (Figure S8c,f,i, labeled as c, f, and i in Figure 5, respectively), the increasing energy position of VBM (K) can be indicated by the absence of two minor hybridization orbitals near the top oxygen atomic layers. Increasing in-plane atomic distance leads to the weakening of orbital hybridization, further resulting in a less stable and higher-energy status.[61] Thus, the energy position of VBM (K) shows a similar variation trend to VBM (Γ). Since the spatial distribution of VBM (K) is wider than that of VBM (Γ), if we compare Figure S8e,f, VBM (K) is more sensitive to strain, which explains the more rapid variation of VBM (K) than VBM (Γ) in Figure 5.

Figure 6a shows the electrostatic potential curves of relaxed and strained $Ga_2O_3$ monolayers along the $z$ direction. The variation of ΔΦ versus lattice distortion is shown in Figure 5.

At the relaxed status, ΔΦ reaches 3.47 eV by the HSE functional calculation, much larger than that of the other 2D $Ga_2X_3$ family members ($Ga_2S_3$, 1.65 eV; $Ga_2Se_3$, 1.30 eV; $Ga_2Te_3$, 0.88 eV) and also larger than $\alpha$-$In_2Se_3$ (1.38 eV),[5] even though they share the same structural configuration. The largest ΔΦ of $Ga_2O_3$ among the 2D $Ga_2X_3$ monolayers could originate from the largest electronegativity of oxygen in the group VI. Figure 6b shows the variation of the dipole moment of the $Ga_2O_3$ monolayer with lattice distortion. With decreasing compressive strain and increasing tensile strain, the dipole moment keeps increasing. A similar variation of the dipole moment versus in-plane strain can also be seen in $\alpha$-$In_2Se_3$.[22] Since the dipole moment is introduced from the asymmetric configuration between top and bottom O−Ga−O trilayers, we studied the relative thickness between these two trilayers ($T_{top}$ and $T_{bottom}$ in Figure 6b, respectively) as shown in Figure 6b. Interestingly, with decreasing compressive strain and increasing tensile strain, the ratio of $T_{top}$ and $T_{bottom}$ ($T_{top}/T_{bottom}$) keeps decreasing. Since top and bottom O−Ga−O trilayers act as negative and positive charge centers, respectively, the spatial separation of positive and negative charge centers becomes more intense, leading to larger dipole moment.

Since the $Ga_2O_3$ monolayer changes from direct band gap to indirect band gap with VBM changing from Γ to K point when decreasing compressive strain and increasing tensile strain, we compared the charge distribution of $Ga_2O_3$ with direct and indirect band gap characteristics under the corresponding distortion, as shown in Figure 6c,d. It can be seen that despite the difference in band gap characteristics, due to the asymmetric configuration, CBM and VBM tend to locate on opposite sides of the monolayer. Spatial charge distributions of the $Ga_2O_3$ monolayer from −4 to 6% are presented in Figure S10. When $Ga_2O_3$ is a direct band gap semiconductor, the spatial separation of CBM and VBM is more intense (Figure 6c) than when it is an indirect band gap material (Figures 6d

**Table 1. Calculated Electron Mobility $\mu$ (cm$^2$ V$^{-1}$ s$^{-1}$) of the Ga$_2$O$_3$ Monolayer along the $x$ and $y$ Directions[a]**

| lattice distortion | $m_x^*$ ($m_0$)/$m_y^*$ ($m_0$) | $E_{1x}$ (eV) | $E_{1y}$ (eV) | $C_{2D-x}$ (J/m$^2$) | $C_{2D-y}$ (J/m$^2$) | $\mu_x$ (cm$^2$ V$^{-1}$ s$^{-1}$) | $\mu_y$ (cm$^2$ V$^{-1}$ s$^{-1}$) |
|---|---|---|---|---|---|---|---|
| −6% | 0.426 | 2.294 | 2.315 | | | 4182 | 4421 |
| −4% | 0.397 | 1.919 | 1.837 | | | 6880 | 7414 |
| −2% | 0.374 | −2.034 | −1.948 | | | 6901 | 7429 |
| 0 | 0.356 | −2.294 | −2.249 | 187.193 | 184.832 | 5988 | 6153 |
| 2% | 0.340 | −3.320 | −3.335 | | | 3134 | 3067 |
| 4% | 0.326 | −4.164 | −4.381 | | | 2167 | 1933 |
| 6% | 0.312 | −5.166 | −5.018 | | | 1537 | 1609 |

[a]Effective electron mass is labeled as $m^*$ ($m_0$), $E_1$ represents the deformation potential constant (eV), and $C_{2D}$ represents the elastic coefficient (J/m$^2$). Note that all of the calculations here use the HSE hybrid functional.
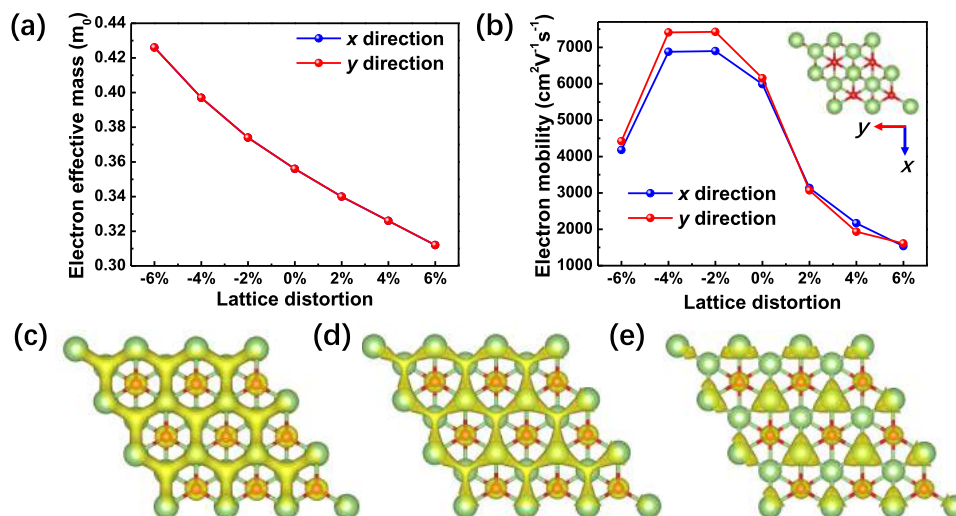


**Figure 7.** (a) Electron effective masses and (b) room-temperature electron mobility of the Ga$_2$O$_3$ monolayer versus lattice distortions. Partial charge distribution at CBM ($\Gamma$) with lattice distortions of (c) −4%, (d) 0, and (e) 6%. All three figures are shown at the same isosurface level.

and S11). For potential applications of energy conversion such as photocatalysis and photodetection, it benefits to decreasing recombination probability that the photon-generated electrons and holes scatter in different areas of the materials.[5]

**3.3. Strain-Engineered Carrier Mobility.** For potential applications in electronic devices, it is of great importance to evaluate the carrier transport ability (i.e., effective mass and mobility) of the Ga$_2$O$_3$ monolayer. The electron and hole effective masses are calculated by the parabola fitting of the band curves near the CBM ($\Gamma$) and VBM, respectively, in units of free electron mass $m_0$. For the relaxed Ga$_2$O$_3$ monolayer, the calculated electron effective masses are 0.356 $m_0$ along all directions (i.e., isotropic), while the calculated hole effective masses are more than 20 times higher than the electron effective masses, as shown in Figure S12a,b, indicated by the much flatter band curve of VBM in Figure 2a. Besides, the isotropic feature of electrons at CBM ($\Gamma$) and anisotropic feature of holes at VBM (K) can also be indicated by the 3D band diagram (Figure S12). In general, larger effective mass results in lower carrier mobility, so hole mobility is far much lower than electron mobility. Thus, detailed discussions of electron mobility are presented herein.

The electron mobility ($\mu_{2D}$) of 2D semiconductor materials can be calculated based on the deformation potential theory as follows:[62,63]

$$\mu_{2D} = \frac{e\hbar^3 C_{2D}}{k_B T m^* m_d E_1^2} \quad (1)$$

where $e$ is the electron charge, $\hbar$ is the reduced Planck constant, $k_B$ is the Boltzmann constant, and $T$ is the temperature, which is set to be 300 K to represent room temperature ambient. $m_d$ is the average effective mass, which can be calculated by $m_d = \sqrt{m_x^* m_y^*}$. $C_{2D}$ is the elastic modulus and can be calculated by

$$C_{2D} = \frac{1}{S_0} \frac{\partial^2 E}{\partial \left(\frac{\Delta l}{l_0}\right)^2} \quad (2)$$

where $E$ is the total energy of the system, $l_0$ is the lattice constant, $\Delta l$ is its lattice deformation, and $S_0$ is the area of the optimized lattice. $m^*$ is the electron effective mass calculated along the $x$ and $y$ directions, respectively. $E_1$ is the deformation potential constant, calculated by $E_1 = \Delta V/(\Delta l/l_0)$, where $\Delta V$ is the energy difference of CBM ($\Gamma$) induced by lattice distortion. In principle, calculating the practical electron−phonon matrix is more rigorous and accurate than the deformation potential theory, but it is highly time-consuming. The deformation potential theory is a more efficient method, which has been widely used in calculating the intrinsic mobility.[62,63] The details on the calculation of elastic constants, deformation potentials, as well as the estimated errors are summarized in Table 1 and Figure S13. It is noted that the estimated error of $E_1$ is smaller than 12%, so the obtained results are well acceptable.[63]

Figure 7a,b shows the calculated electron effective mass and mobility versus lattice distortions, respectively. It should be
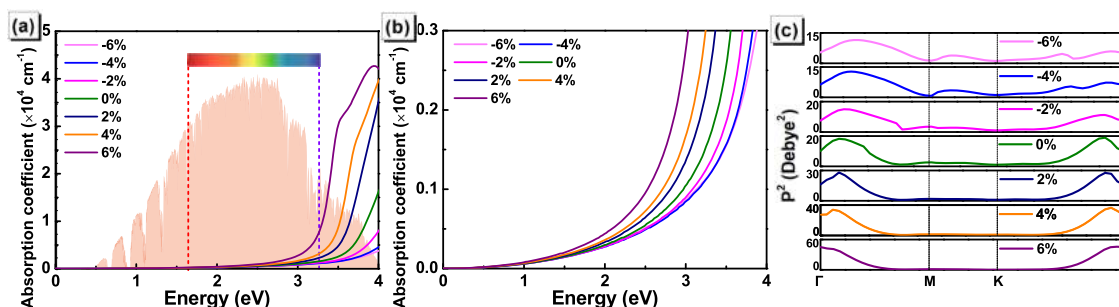
**Figure 8.** (a) Optical absorption spectra of the $Ga_2O_3$ monolayer and solar radiation spectrum (red areas). The AM 1.5G solar radiation spectrum is taken from NREL website (https://www.nrel.gov/grid/solar-resource/spectra-am1.5.html), with respect to the standards (ASTM G173-03 global[67] and IEC 60904-3[68]). (b) Amplified absorption spectra. (c) Transition dipole moment of the $Ga_2O_3$ monolayer with different lattice distortions.

noticed that the calculated electron effective masses along $\Gamma-$K and $\Gamma-$M are almost the same (i.e., isotropic) even with different biaxial strain engineering, together with the electron mobility along the $x$ and $y$ directions, which indicates a weak electronic anisotropy of the 2D $Ga_2O_3$ monolayer, similar to the $\alpha$-$In_2Se_3$ case.[64] The calculated values of $C_{2D}$ along the $x$ and $y$ directions are similar, resulting from the same values of lattice constants of the in-plane $a$ and $b$ directions.[15] Interestingly, this electronic and mechanical isotropy can be also seen in other 2D $M_2X_3$ family members with the same atomic configuration, such as $Ga_2S_3$, $Ga_2Se_3$, $In_2S_3$, and $In_2Te_3$.[5] The common feature of these 2D $M_2X_3$ materials is that their CBM always locates on $\Gamma$ point with different biaxial strains. What is more, from +6 to −4% lattice distortion, with decreasing tensile strain and increasing compressive strain, electron mobility keeps increasing, which originates from the low absolute values of the deformation potential constant ($E_1$) in the region of compressive strain, as shown in Table 1. As a result, the electron mobility of the $Ga_2O_3$ monolayer reaches ~7000 $cm^2$ $V^{-1}$ $s^{-1}$ with a lattice distortion of −4%. The decrease in mobility at −6% is likely to be from the corruption of stability at the extreme compressive status. Even at the extremely stretched status, the electron mobility is still larger than 1000 $cm^2$ $V^{-1}$ $s^{-1}$, which exceeds those of the monolayers of $MoS_2$ (~200 $cm^2$ $V^{-1}$ $s^{-1}$)[65] and GaN (~300 $cm^2$ $V^{-1}$ $s^{-1}$)[66] and is comparable to those of $\alpha$-$In_2Se_3$ (1.04 × $10^3$ $cm^2$ $V^{-1}$ $s^{-1}$) and $\beta$-$In_2Se_3$ (1.39 × $10^3$ $cm^2$ $V^{-1}$ $s^{-1}$).[64] Owing to its outstanding electron mobility, the $Ga_2O_3$ monolayer is well qualified in applications of nanoscale electronic devices. The hole mobility is also calculated, which is obviously smaller compared with the electron mobility, as shown in Table S1.

To have a deeper insight into the influence of lattice distortion on electron mobility and to explain the extremely high electron mobility with −4% compressive strain, we investigated the spatial charge distribution at CBM ($\Gamma$) of the $Ga_2O_3$ monolayer with different lattice distortions, as shown in Figure 7c−e. With decreasing distances between the neighboring gallium and oxygen atoms, overlapping of wavefunctions and the bonding characteristics are strongly enhanced, as shown by the yellow triangular cross-linking regions in Figure 7c,d. This can explain the increasing electron mobility when increasing compressive strain. Similarly, low deformation potential constant (absolute value) and high mobility under extreme compressive strain condition are also seen in the monoclinic $\beta$-$Ga_2O_3$ monolayer.[16]

**3.4. Strain-Engineered Optical Properties.** To evaluate the light absorption ability, we studied the absorption spectra

of the $Ga_2O_3$ monolayer with different lattice distortions, as shown in Figure 8a. The absorption spectra are calculated from the imaginary part of the complex dielectric function $\varepsilon(\omega) = \varepsilon_1(\omega) + i\varepsilon_2(\omega)$, and the absorption coefficient could be obtained from calculating $\alpha(E) = (\sqrt{2}\omega/c)\{[(\varepsilon_1^2 + \varepsilon_2^2)^{1/2} - \varepsilon_1]\}^{1/2}$ as described in ref 43. In energy regions near the absorption edge from 2 eV to 3 eV, as shown in Figure 8b, with decreasing compressive strain and increasing tensile strain, absorption edge exhibits blueshift first and then redshift, in good accordance with the band gap variation. The absorption tail below the band gap is owing to the smearing effect in the calculation, which determines how the partial occupancies are set for each wavefunction, and can be considered as the temperature effect in experiments. The absorption tail is also observed in previous reports.[6,63]

As shown in Figure 8a, when tensile strain is applied to the $Ga_2O_3$ monolayer, much-enhanced light absorption can be observed in energy regions below 4 eV, where the solar radiation is strong (red areas in Figure 8a). This is owing to the gap narrowing by strain engineering. What is more, if an extreme tensile strain of +6% lattice distortion is applied, the absorption ability is several times higher, which can be used as excellent photoabsorber. The strong solar radiation absorption of the $Ga_2O_3$ monolayer makes it promising in photocatalytic applications.[5,30,43] For many 2D materials, the large exciton binding energy will prevent the separation of electrons and holes. However, in this novel $Ga_2O_3$ monolayer, the intrinsic electric field is introduced by the intrinsic dipole because of its asymmetric atomic configuration. Such an intrinsic polarization may bring benefits to the separation of photogenerated electrons and holes, which has been theoretically studied in many novel asymmetric 2D materials.[5,6,30,52] It should also be noted that the intrinsic polarization correlated with photo-catalyst activity, such as water splitting, has been widely studied theoretically and verified experimentally in ferroelectric materials, which also feature an intrinsic electric field.[53,54] The presence of the internal field provides a driving force for electrons and holes to move in the opposite directions, thus separating the carriers. As a result, the CBM and VBM wavefunctions spatially localize at the opposite sides, as shown in Figures 2c,d and 6. From this aspect of view, the novel $Ga_2O_3$ monolayer with similar characteristics shows advantages and potentials in energy conversion such as photocatalytic water splitting and photodetection.

The squared dipole transition matrix elements ($P^2$) were calculated to reveal the transition probability of electrons between VBM and CBM at different $k$ points,[69] which

evaluates whether the incident light can be absorbed by the semiconductor, shown in Figure 8c. It is obvious that transition at $\Gamma$ point is always allowed at different lattice distortions. Besides, decreasing compressive strain and increasing tensile strain lead to higher $P^2$ at $\Gamma$ point. This originates from the increasing orbital overlapping of the electrons and holes,[70] as illustrated in Figure S10 with CBM ($\Gamma$) and VBM ($\Gamma$) wavefunctions. As a result, the allowed optical transition of electrons from VBM to CBM guarantees excellent optoelectronic applications.

## 4. CONCLUSIONS

In conclusion, we systemically study the electronic, carrier transport, and optical properties of the novel $Ga_2O_3$ monolayer with the FE-ZB′ configuration using first-principles calculations. Excellent dynamic and thermodynamic stability of the studied $Ga_2O_3$ is demonstrated by phonon dispersion and AIMD verifications. Indirect-to-direct transition and enhanced electron mobility can be realized by biaxial strain engineering. The intrinsic dipole induced in the asymmetric $Ga_2O_3$ monolayer guarantees its strong ability to boost the separation of holes and electrons within the quintuple-layer structure. As a result, CBM and VBM locate on opposite sides of the $Ga_2O_3$ monolayer. The tunable properties of the $Ga_2O_3$ monolayer indicate that when compressive strain is applied to the $Ga_2O_3$ monolayer, it still has suitable band gap values and outstanding carrier transport ability, promising for the flexible power devices. When tensile strain is applied, the stretched $Ga_2O_3$ monolayer exhibits enhanced optical absorption, extending the range from the UV to visible light region, guaranteeing its potential applications in optoelectronic devices and energy conversion such as photocatalytic water splitting. These tunable properties certify the wide application ranges of our studied novel $Ga_2O_3$ monolayer.

## ■ ASSOCIATED CONTENT

### ⑤ Supporting Information

The Supporting Information is available free of charge at https://pubs.acs.org/doi/10.1021/acsami.0c04173.

Comparison of the $Ga_2O_3$ monolayer with $\beta$-$Ga_2O_3$; projected band structures; demonstration of room-temperature stability; variation of deformation energy and monolayer thickness under different strains; phonon dispersion spectra and AIMD simulations of the extremely strained $Ga_2O_3$ monolayer; shift of band edge and band gap with respect to different vacuum levels; band gap values calculated by different functionals; CBM and VBM wavefunctions of the $Ga_2O_3$ monolayer under different strains; partial charge distributions of different lattice distortions; angular-dependent effective mass and 3D band diagram of the relaxed $Ga_2O_3$ monolayer; mobility calculation process and error estimation; and hole mobility calculation (PDF)

## ■ AUTHOR INFORMATION

### Corresponding Authors

**Zhaofu Zhang** − *Department of Engineering, Cambridge University, Cambridge CB2 1PZ, United Kingdom;* ⓘ orcid.org/0000-0002-1406-1256; Email: zz389@cam.ac.uk

**Mengyuan Hua** − *Department of Electrical and Electronic Engineering, Southern University of Science and Technology, Shenzhen 518055, China;* Email: huamy@sustech.edu.cn

### Authors

**Yikai Liao** − *Department of Electrical and Electronic Engineering, Southern University of Science and Technology, Shenzhen 518055, China;* ⓘ orcid.org/0000-0002-7046-8819

**Zhibin Gao** − *Department of Physics, National University of Singapore, Singapore 117551, Republic of Singapore;* ⓘ orcid.org/0000-0002-6843-381X

**Qingkai Qian** − *Department of Electrical Engineering, The Pennsylvania State University, University Park, Pennsylvania 16802, United States;* ⓘ orcid.org/0000-0001-7513-0676

Complete contact information is available at:
https://pubs.acs.org/10.1021/acsami.0c04173

### Author Contributions

▽Y.L. and Z.Z. contributed equally to this work.

### Notes

The authors declare no competing financial interest.

## ■ ACKNOWLEDGMENTS

## ■ REFERENCES

(1) Tsao, J. Y.; Chowdhury, S.; Hollis, M. A.; Jena, D.; Johnson, N. M.; Jones, K. A.; Kaplar, R. J.; Rajan, S.; Van de Walle, C. G.; Bellotti, E.; Chua, C. L.; Collazo, R.; Coltrin, M. E.; Cooper, J. A.; Evans, K. R.; Graham, S.; Grotjohn, T. A.; Heller, E. R.; Higashiwaki, M.; Islam, M. S.; Juodawlkis, P. W.; Khan, M. A.; Koehler, A. D.; Leach, J. H.; Mishra, U. K.; Nemanich, R. J.; Pilawa-Podgurski, R. C. N.; Shealy, J. B.; Sitar, Z.; Tadjer, M. J.; Witulski, A. F.; Wraback, M.; Simmons, J. A. Ultrawide-Bandgap Semiconductors: Research Opportunities and Challenges. *Adv. Electron. Mater.* **2018**, *4*, No. 1600501.

(2) Pearton, S. J.; Yang, J.; Cary, P. H.; Ren, F.; Kim, J.; Tadjer, M. J.; Mastro, M. A. A Review of $Ga_2O_3$ Materials, Processing, and Devices. *Appl. Phys. Rev.* **2018**, *5*, No. 011301.

(3) Singh, A. K.; Mathew, K.; Zhuang, H. L.; Hennig, R. G. Computational Screening of 2D Materials for Photocatalysis. *J. Phys. Chem. Lett.* **2015**, *6*, 1087−1098.

(4) Mounet, N.; Gibertini, M.; Schwaller, P.; Campi, D.; Merkys, A.; Marrazzo, A.; Sohier, T.; Castelli, I. E.; Cepellotti, A.; Pizzi, G.; Marzari, N. Two-Dimensional Materials from High-Throughput Computational Exfoliation of Experimentally Known Compounds. *Nat. Nanotechnol.* **2018**, *13*, 246−252.

(5) Fu, C. F.; Sun, J.; Luo, Q.; Li, X.; Hu, W.; Yang, J. Intrinsic Electric Fields in Two-Dimensional Materials Boost the Solar-to-Hydrogen Efficiency for Photocatalytic Water Splitting. *Nano Lett.* **2018**, *18*, 6312−6317.

(6) Xia, C.; Xiong, W.; Du, J.; Wang, T.; Peng, Y.; Li, J. Universality of Electronic Characteristics and Photocatalyst Applications in the Two-Dimensional Janus Transition Metal Dichalcogenides. *Phys. Rev. B* **2018**, *98*, No. 165424.

(7) Rogers, J. A.; Someya, T.; Huang, Y. Materials and Mechanics for Stretchable Electronics. *Science* **2010**, *327*, 1603−1607.

(8) Kang, P.; Wang, M. C.; Knapp, P. M.; Nam, S. Crumpled Graphene Photodetector with Enhanced, Strain-Tunable, and Wavelength-Selective Photoresponsivity. *Adv. Mater.* **2016**, *28*, 4639−4645.

(9) Lee, S. K.; Kim, B. J.; Jang, H.; Yoon, S. C.; Lee, C.; Hong, B. H.; Rogers, J. A.; Cho, J. H.; Ahn, J. H. Stretchable Graphene Transistors with Printed Dielectrics and Gate Electrodes. *Nano Lett.* **2011**, *11*, 4642−4646.

(10) Claeyssens, F.; Freeman, C. L.; Allan, N. L.; Sun, Y.; Ashfold, M. N. R.; Harding, J. H. Growth of ZnO Thin Films—Experiment and Theory. *J. Mater. Chem.* **2005**, *15*, 139−148.

(11) Tusche, C.; Meyerheim, H. L.; Kirschner, J. Observation of Depolarized ZnO(0001) Monolayers: Formation of Unreconstructed Planar Sheets. *Phys. Rev. Lett.* **2007**, *99*, No. 026102.

(12) Zhuang, H. L.; Singh, A. K.; Hennig, R. G. Computational Discovery of Single-Layer III-V Materials. *Phys. Rev. B* **2013**, *87*, No. 165415.

(13) Al Balushi, Z. Y.; Wang, K.; Ghosh, R. K.; Vila, R. A.; Eichfeld, S. M.; Caldwell, J. D.; Qin, X.; Lin, Y. C.; DeSario, P. A.; Stone, G.; Subramanian, S.; Paul, D. F.; Wallace, R. M.; Datta, S.; Redwing, J. M.; Robinson, J. A. Two-Dimensional Gallium Nitride Realized via Graphene Encapsulation. *Nat. Mater.* **2016**, *15*, 1166−1171.

(14) Peelaers, H.; Van de Walle, C. G. Lack of Quantum Confinement in Ga$_2$O$_3$ Nanolayers. *Phys. Rev. B* **2017**, *96*, No. 081409.

(15) Su, J.; Guo, R.; Lin, Z.; Zhang, S.; Zhang, J.; Chang, J.; Hao, Y. Unusual Electronic and Optical Properties of Two-Dimensional Ga$_2$O$_3$ Predicted by Density Functional Theory. *J. Phys. Chem. C* **2018**, *122*, 24592−24599.

(16) Guo, R.; Su, J.; Lin, Z.; Zhang, J.; Qin, Y.; Zhang, J.; Chang, J.; Hao, Y. Understanding the Potential of 2D Ga$_2$O$_3$ in Flexible Optoelectronic Devices: Impact of Uniaxial Strain and Electric Field. *Adv. Theory Simul.* **2019**, *2*, No. 1900106.

(17) Wei, Y.; Liu, C.; Zhang, Y.; Qi, C.; Li, H.; Wang, T.; Ma, G.; Liu, Y.; Dong, S.; Huo, M. Modulation of Electronic and Optical Properties by Surface Vacancies in Low-Dimensional β-Ga$_2$O$_3$. *Phys. Chem. Chem. Phys.* **2019**, *21*, 14745−14752.

(18) Zhou, H.; Maize, K.; Qiu, G.; Shakouri, A.; Ye, P. D. β-Ga$_2$O$_3$ on Insulator Field-Effect Transistors with Drain Currents Exceeding 1.5 A/mm and Their Self-Heating Effect. *Appl. Phys. Lett.* **2017**, *111*, No. 092210.

(19) Kwon, Y.; Lee, G.; Oh, S.; Kim, J.; Pearton, S. J.; Ren, F. Tuning the Thickness of Exfoliated Quasi-Two-Dimensional β-Ga$_2$O$_3$ Flakes by Plasma Etching. *Appl. Phys. Lett.* **2017**, *110*, No. 131901.

(20) Barman, S. K.; Huda, M. N. Mechanism Behind the Easy Exfoliation of Ga$_2$O$_3$ Ultra-Thin Film Along (100) Surface. *Phys. Status Solidi RRL* **2019**, *13*, No. 1800554.

(21) Jacobs-Gedrim, R. B.; Shanmugam, M.; Jain, N.; Durcan, C. A.; Murphy, M. T.; Murray, T. M.; Matyi, R. J.; Moore, R. L., 2nd; Yu, B. Extraordinary Photoresponse in Two-Dimensional In$_2$Se$_3$ Nanosheets. *ACS Nano* **2014**, *8*, 514−521.

(22) Ding, W.; Zhu, J.; Wang, Z.; Gao, Y.; Xiao, D.; Gu, Y.; Zhang, Z.; Zhu, W. Prediction of Intrinsic Two-Dimensional Ferroelectrics in In$_2$Se$_3$ and Other III$_2$-VI$_3$ Van der Waals Materials. *Nat. Commun.* **2017**, *8*, No. 14956.

(23) Xiao, J.; Zhu, H.; Wang, Y.; Feng, W.; Hu, Y.; Dasgupta, A.; Han, Y.; Wang, Y.; Muller, D. A.; Martin, L. W.; Hu, P.; Zhang, X. Intrinsic Two-Dimensional Ferroelectricity with Dipole Locking. *Phys. Rev. Lett.* **2018**, *120*, No. 227601.

(24) Cui, C.; Hu, W. J.; Yan, X.; Addiego, C.; Gao, W.; Wang, Y.; Wang, Z.; Li, L.; Cheng, Y.; Li, P.; Zhang, X.; Alshareef, H. N.; Wu, T.; Zhu, W.; Pan, X.; Li, L. J. Intercorrelated In-Plane and Out-of-Plane Ferroelectricity in Ultrathin Two-Dimensional Layered Semiconductor In$_2$Se$_3$. *Nano Lett.* **2018**, *18*, 1253−1258.

(25) Zhao, P.; Ma, Y.; Lv, X.; Li, M.; Huang, B.; Dai, Y. Two-Dimensional III$_2$-VI$_3$ Materials: Promising Photocatalysts for Overall Water Splitting under Infrared Light Spectrum. *Nano Energy* **2018**, *51*, 533−538.

(26) Xie, Z.; Yang, F.; Xu, X.; Lin, R.; Chen, L. Functionalization of α-In$_2$Se$_3$ Monolayer via Adsorption of Small Molecule for Gas Sensing. *Front. Chem.* **2018**, *6*, 430.

(27) Xue, F.; Zhang, J.; Hu, W.; Hsu, W. T.; Han, A.; Leung, S. F.; Huang, J. K.; Wan, Y.; Liu, S.; Zhang, J.; He, J. H.; Chang, W. H.; Wang, Z. L.; Zhang, X.; Li, L. J. Multidirection Piezoelectricity in Mono- and Multilayered Hexagonal α-In$_2$Se$_3$. *ACS Nano* **2018**, *12*, 4976−4983.

(28) Sun, Z.; Liao, T.; Dou, Y.; Hwang, S. M.; Park, M. S.; Jiang, L.; Kim, J. H.; Dou, S. X. Generalized Self-Assembly of Scalable Two-Dimensional Transition Metal Oxide Nanosheets. *Nat. Commun.* **2014**, *5*, No. 3813.

(29) Demirci, S.; Avazlı, N.; Durgun, E.; Cahangirov, S. Structural and Electronic Properties of Monolayer Group III Monochalcogenides. *Phys. Rev. B* **2017**, *95*, No. 115409.

(30) Ji, Y.; Yang, M.; Lin, H.; Hou, T.; Wang, L.; Li, Y.; Lee, S. Janus Structures of Transition Metal Dichalcogenides as the Heterojunction Photocatalysts for Water Splitting. *J. Phys. Chem. C* **2018**, *122*, 3123−3129.

(31) Peimyoo, N.; Barnes, M.; Mehew, J.; De Sanctis, A.; Amit, I.; Escloar, J.; Anastasiou, K.; Rooney, A.; Haigh, S.; Russo, S.; Cracium, M.; Withers, F. Laser-Writable High-*k* Dielectric for Van Der Waals Nanoelectronics. *Sci. Adv.* **2019**, *5*, No. eaau0906.

(32) Cartamil-Bueno, S.; Steeneken, P.; Tichelaar, F.; Navarro-Moratalla, E.; Venstra, W.; van Leeuwen, R.; Coronado, E.; van der Zant, H.; Steele, G.; Castellanos-Gomez, A. High-Quality-Factor Tantalum Oxide Nanomechanical Resonators by Laser Oxidation of TaSe$_2$. *Nano Res.* **2015**, *8*, 2842−2849.

(33) Du, Z.; Yang, S.; Li, S.; Lou, J.; Zhang, S.; Wang, S.; Li, B.; Gong, Y.; Song, L.; Zou, X.; Ajayan, P. M. Conversion of Non-Van Der Waals Solids to 2D Transition-Metal Chalcogenides. *Nature* **2020**, *577*, 492−496.

(34) Kresse, G.; Furthmuller, J. Efficient Iterative Schemes for ab initio Total-Energy Calculations Using a Plane-Wave Basis Set. *Phys. Rev. B* **1996**, *54*, 11169−11186.

(35) Blöchl, P. E. Projector Augmented-Wave Method. *Phys. Rev. B* **1994**, *50*, 17953−17979.

(36) Kresse, G.; Joubert, D. From Ultrasoft Pseudopotentials to the Projector Augmented-Wave Method. *Phys. Rev. B* **1999**, *59*, 1758−1775.

(37) Willand, A.; Kvashnin, Y. O.; Genovese, L.; Vazquez-Mayagoitia, A.; Deb, A. K.; Sadeghi, A.; Deutsch, T.; Goedecker, S. Norm-Conserving Pseudopotentials with Chemical Accuracy Compared to All-Electron Calculations. *J. Chem. Phys.* **2013**, *138*, No. 104109.

(38) Adolph, B.; Furthmüller, J.; Bechstedt, F. Optical Properties of Semiconductors Using Projector-Augmented Waves. *Phys. Rev. B* **2001**, *63*, No. 125108.

(39) Perdew, J. P.; Burke, K.; Ernzerhof, M. Generalized Gradient Approximation Made Simple. *Phys. Rev. Lett.* **1996**, *77*, 3865−3868.

(40) Heyd, J.; Peralta, J. E.; Scuseria, G. E.; Martin, R. L. Energy Band Gaps and Lattice Parameters Evaluated with the Heyd-Scuseria-Ernzerhof Screened Hybrid Functional. *J. Chem. Phys.* **2005**, *123*, No. 174101.

(41) Heyd, J.; Scuseria, G. E.; Ernzerhof, M. Erratum: "Hybrid Functionals Based on a Screened Coulomb Potential" [J. Chem. Phys. 118, 8207 (2003)]. *J. Chem. Phys.* **2006**, *124*, No. 219906.

(42) Grimme, S.; Antony, J.; Ehrlich, S.; Krieg, H. A Consistent and Accurate ab initio Parametrization of Density Functional Dispersion Correction (DFT-D) for the 94 Elements H-Pu. *J. Chem. Phys.* **2010**, *132*, No. 154104.

(43) Zhang, Z.; Qian, Q.; Li, B.; Chen, K. J. Interface Engineering of Monolayer MoS$_2$/GaN Hybrid Heterostructure: Modified Band Alignment for Photocatalytic Water Splitting Application by Nitridation Treatment. *ACS Appl. Mater. Interfaces* **2018**, *10*, 17419−17426.

(44) Wang, V.; Xu, N.; Liu, J. C.; Tang, G.; Geng, W. T. VASPKIT: A Pre- and Post-Processing Program for VASP Code. 2019,

ArXiv:1908.08269. https://arxiv.org/abs/1908.08269 (accessed on 25 August 2019).

(45) Baroni, S.; de Gironcoli, S.; Dal Corso, A.; Giannozzi, P. Phonons and Related Crystal Properties from Density-Functional Perturbation Theory. *Rev. Mod. Phys.* **2001**, *73*, 515−562.

(46) Togo, A.; Oba, F.; Tanaka, I. First-Principles Calculations of the Ferroelastic Transition Between Rutile-Type and CaCl$_2$-Type SiO$_2$ at High Pressures. *Phys. Rev. B* **2008**, *78*, No. 134106.

(47) Zhang, Z.; Huang, B.; Qian, Q.; Gao, Z.; Tang, X.; Li, B. Strain-Tunable III-Nitride/ZnO Heterostructures for Photocatalytic Water-Splitting: A Hybrid Functional Calculation. *APL Mater.* **2020**, *8*, No. 041114.

(48) Lu, A. Y.; Zhu, H.; Xiao, J.; Chuu, C. P.; Han, Y.; Chiu, M. H.; Cheng, C. C.; Yang, C. W.; Wei, K. H.; Yang, Y.; Wang, Y.; Sokaras, D.; Nordlund, D.; Yang, P.; Muller, D. A.; Chou, M. Y.; Zhang, X.; Li, L. J. Janus Monolayers of Transition Metal Dichalcogenides. *Nat. Nanotechnol.* **2017**, *12*, 744−749.

(49) Peng, R.; Ma, Y.; Zhang, S.; Huang, B.; Kou, L.; Dai, Y. Self-Doped P−N Junctions in Two-Dimensional In2X3 Van Der Waals Materials. *Mater. Horiz.* **2020**, *7*, 504−510.

(50) Shao, Y.; Wang, Q.; Pan, H.; Shi, X. Van Der Waals Contact to 2D Semiconductors with a Switchable Electric Dipole: Achieving Both n- and p- Type Ohmic Contacts to Metals with a Wide Range of Work Functions. *Adv. Electron. Mater.* **2020**, *6*, No. 1900981.

(51) Yin, W.; Wen, B.; Nie, G.; Wei, X.; Liu, L. Tunable Dipole and Carrier Mobility for a Few Layer Janus MoSSe Structure. *J. Mater. Chem. C* **2018**, *6*, 1693−1700.

(52) Ma, X. C.; Wu, X.; Wang, H. D.; Wang, Y. C. A Janus MoSSe Monolayer: a Potential Wide Solar-Spectrum Water-Splitting Photocatalyst with a Low Carrier Recombination Rate. *J. Mater. Chem. A* **2018**, *6*, 2295−2301.

(53) Khan, M. A.; Nadeem, M. A.; Idriss, H. Ferroelectric Polarization Effect on Surface Chemistry and Photo-Catalytic Activity: A Review. *Surf. Sci. Rep.* **2016**, *71*, 1−31.

(54) Li, L.; Salvador, P. A.; Rohrer, G. S. Photocatalysts with Internal Electric Fields. *Nanoscale* **2014**, *6*, 24−42.

(55) Yun, W. S.; Han, S. W.; Hong, S. C.; Kim, I. G.; Lee, J. D. Thickness and Strain Effects on Electronic Structures of Transition Metal Dichalcogenides: 2H-MX$_2$ Semiconductors (M = Mo, W; X = S, Se, Te). *Phys. Rev. B* **2012**, *85*, No. 033305.

(56) Tamleh, S.; Rezaei, G.; Vaseghi, B.; Jalilian, J. Electronic Structure and Optical Properties of Two-Dimensional Tetragonal and Hexagonal ScN Monolayers: Impact of Strain. *J. Phys. Chem. Solids* **2020**, *138*, No. 109270.

(57) Lloyd, D.; Liu, X.; Christopher, J. W.; Cantley, L.; Wadehra, A.; Kim, B. L.; Goldberg, B. B.; Swan, A. K.; Bunch, J. S. Band Gap Engineering with Ultralarge Biaxial Strains in Suspended Monolayer MoS$_2$. *Nano Lett.* **2016**, *16*, 5836−41.

(58) Hedin, L. New Method for Calculating the One-Particle Green's Function with Application to the Electron-Gas Problem. *Phys. Rev.* **1965**, *139*, A796−A823.

(59) Peng, X.; Wei, Q.; Copple, A. Strain-Engineered Direct-Indirect Band Gap Transition and its Mechanism in Two-Dimensional Phosphorene. *Phys. Rev. B* **2014**, *90*, No. 085402.

(60) Li, Y.; Yang, S.; Li, J. Modulation of the Electronic Properties of Ultrathin Black Phosphorus by Strain and Electrical Field. *J. Phys. Chem. C* **2014**, *118*, 23970−23976.

(61) Jin, H.; Li, J.; Dai, Y.; Wei, Y. Engineering the Electronic and Optoelectronic Properties of InX (X = S, Se, Te) Monolayers via Strain. *Phys. Chem. Chem. Phys.* **2017**, *19*, 4855−4860.

(62) Bardeen, J.; Shockley, W. Deformation Potentials and Mobilities in Non-Polar Crystals. *Phys. Rev.* **1950**, *80*, 72−80.

(63) Qiao, J.; Kong, X.; Hu, Z. X.; Yang, F.; Ji, W. High-Mobility Transport Anisotropy and Linear Dichroism in Few-Layer Black Phosphorus. *Nat. Commun.* **2014**, *5*, No. 4475.

(64) Li, X.; Zuo, X.; Li, H.; Han, L.; Gao, Q.; Li, D.; Cui, B.; Liu, D.; Qu, F. Exotic Magnetism in As-doped $\alpha/\beta$-In$_2$Se$_3$ Monolayers with Tunable Anisotropic Carrier Mobility. *Phys. Chem. Chem. Phys.* **2019**, *21*, 19234−19241.

(65) Cai, Y.; Zhang, G.; Zhang, Y. W. Polarity-Reversed Robust Carrier Mobility in Monolayer MoS$_2$ Nanoribbons. *J. Am. Chem. Soc.* **2014**, *136*, 6269−6275.

(66) Tong, L.; He, J.; Yang, M.; Chen, Z.; Zhang, J.; Lu, Y.; Zhao, Z. Anisotropic Carrier Mobility in Buckled Two-Dimensional GaN. *Phys. Chem. Chem. Phys.* **2017**, *19*, 23492−23496.

(67) G03 G173-03, Committee. *Tables for Reference Solar Spectral Irradiances: Direct Normal and Hemispherical on 37 Tilted Surface*; ASTM International: West Conshohocken, PA, 2012.

(68) Standard 60904-3, IEC. *Measurement Principles for Terrestrial Photovoltaic Solar Devices with Reference Spectral Irradiance Data*; International Electrotechnical Commission: Geneva, Switzerland, 2008.

(69) Meng, W.; Wang, X.; Xiao, Z.; Wang, J.; Mitzi, D. B.; Yan, Y. Parity-Forbidden Transitions and Their Impact on the Optical Absorption Properties of Lead-Free Metal Halide Perovskites and Double Perovskites. *J. Phys. Chem. Lett.* **2017**, *8*, 2999−3007.

(70) Luo, J.; Wang, X.; Li, S.; Liu, J.; Guo, Y.; Niu, G.; Yao, L.; Fu, Y.; Gao, L.; Dong, Q.; Zhao, C.; Leng, M.; Ma, F.; Liang, W.; Wang, L.; Jin, S.; Han, J.; Zhang, L.; Etheridge, J.; Wang, J.; Yan, Y.; Sargent, E. H.; Tang, J. Efficient and Stable Emission of Warm-White Light from Lead-Free Halide Double Perovskites. *Nature* **2018**, *563*, 541−545.